Asociación Argentina
de Mecánica Computacional

Mecánica Computacional Vol XLII, pp. 403-412
A. Caggiano, G. Etse, P. Folino, M. Goldschmit, M. Pucheta, M. Storti (Eds.)
L. Battaglia, H. Castro, M. Coussirat, R. Paz, S. Sarraf, A. Scarabino (Issue eds.)
Buenos Aires, November 11-14, 2025

HYDRODYNAMIC SIMULATION OF A POINT ABSORBER WAVE ENERGY CONVERTER USING CFD IN OPENFOAM

Francisco García Almassio[a,b,c], **Alejandro D. Otero** [a,b] **and Roberto Sosa**[a,c]

[a]*Universidad de Buenos Aires, Facultad de Ingeniería, CABA, Argentina, fgarciaa@fi.uba.ar, https://www.fi.uba.ar/*

[b]*Centro de Simulación Computacional, CONICET, CABA, Argentina, aotero@fi.uba.ar, https://csc.conicet.gov.ar/*

[c]*CONICET - Universidad de Buenos Aires. Laboratorio de Ingeniería Naval y Oceánica (LabHiNO), Instituto de Tecnologías y Ciencias de la Ingeniería "Hilario Fernández Long" (INTECIN), Paseo Colón 850, Buenos Aires, C1063, Argentina, rsosa@fi.uba.ar, https://bicyt.conicet.gov.ar/fichas/u/intecin.*

Keywords: WEC, openFOAM, Numerical Wave Tank, Control Strategies.

Abstract. This work presents the development and validation of a hydrodynamic model for a point absorber-type wave energy converter (WEC) using computational fluid dynamics (CFD) within the OpenFOAM framework. The study is performed under monochromatic wave conditions and focuses on the heave response of a buoy. A custom Octree-like meshing strategy was implemented through a combination of polyhedral and hexahedral cells, which reduced computational cost while preserving accuracy in key flow regions. To minimize spurious reflections at the end of the computational domain, a numerical beach was introduced and calibrated using the three-point method, yielding a reflection index as low as 2.3%. The buoy dynamics were investigated under three control scenarios: without control, with resistive, and reactive control strategies. Potential flow results obtained with the open-source solver `Capytaine` were used as reference to derive frequency-dependent hydrodynamic coefficients. The CFD outcomes were compared against `WEC-Sim` predictions, showing consistent agreement with normalized root mean squared errors (nRMSE) below 10% in most cases. These results confirm the robustness of the proposed CFD model and its potential as a complementary tool for the design and analysis of wave energy conversion devices.

ISSN: 2591-3522 DOI: 10.70567/mc.v42.ocsid8209

1 INTRODUCTION

This work presents the development of a hydrodynamic model for a point absorber-type wave energy converter (WEC) using computational fluid dynamics (CFD) within the OpenFOAM framework. The study focuses on the response of a buoy under linear monochromatic wave conditions. Given the absence of native Octree-type meshing tools in OpenFOAM, a custom meshing strategy combining polyhedral and hexahedral cells was implemented. This approach enabled a significant reduction in computational cost while maintaining high accuracy in the most relevant flow regions.

To address undesired wave reflections at the numerical domain boundaries, an absorbing beach was designed and calibrated through the three-point method. The effectiveness of this strategy was validated via reflection tests, which also allowed for the characterization of the buoy's hydrodynamic behavior.

In addition, resistive and reactive control strategies were incorporated into the buoy's power take-off (PTO) system. The resulting performance was compared against `WEC-Sim` predictions (WEC-Sim Development Team, 2025). `WEC-Sim` (Wave Energy Converter SIMulator) is an open-source software for simulating wave energy converters, developed in `Simulink` that solves the governing equation of motion in the time domain, see Eq. (7). Typically, `WEC-Sim` is fed with hydrodynamic coefficients from potential flow solvers such as `Capytaine`, which employs the Boundary Element Method (BEM) to compute added mass, radiation damping, and excitation forces that characterize WEC dynamics (Capytaine Development Team, 2025).

The structure of this paper is as follows: Section 2 introduces the numerical model, Section 3 describes the meshing strategy, Section 4 discusses wave reflection treatment, and Section 5 analyzes the buoy dynamics with and without control.

2 NUMERICAL MODEL

The fluid domain is governed by the incompressible Navier–Stokes equations, enforcing conservation of mass and momentum:

$$\nabla \cdot \mathbf{v} = 0 \tag{1}$$

$$\rho \frac{\partial \mathbf{v}}{\partial t} + \rho\, \mathbf{v} \cdot \nabla \mathbf{v} = -\nabla p + \nabla \cdot \left[\mu \left(\nabla \mathbf{v} + \nabla \mathbf{v}^T\right)\right] + \mathbf{b}. \tag{2}$$

where $\mathbf{v}$ is the velocity field, ρ is the fluid density, p is the pressure field, μ is the dynamic viscosity, and $\mathbf{b}$ represents the external forces (e.g., gravity).

The flow was modelled under laminar conditions, since for buoy's heave motion, the errors introduced by neglecting turbulence are minimal (Windt, 2020), while the computational cost is considerably reduced. The air–water interface was captured through the Volume of Fluid (VoF) method, which resolves a scalar field α representing the phase fraction ($\alpha = 0$ for air and $\alpha = 1$ for water) by means of the transport equation:

$$\frac{\partial \alpha}{\partial t} + \mathbf{v} \cdot \nabla \alpha = 0. \tag{3}$$

The equations are discretized and solved using the finite volume method as implemented in the open-source CFD package OpenFOAM.

The buoy was modelled as a rigid body with a single degree of freedom along the vertical axis. The generalized coordinate is the displacement of the center of mass relative to its equilibrium position:

$$z(t) = z_{CM}(t) - z_{CM}^{(eq)}. \tag{4}$$

From potential flow theory, the WEC dynamics can be represented as:

$$m\,\ddot{z}(t) = f_b(t) + f_r(t) + f_e(t) + f_{PTO}(t), \tag{5}$$

where m is the buoy mass, $f_e(t)$ the excitation force due to the waves, etc., and $f_{PTO}(t)$ the control force applied by the PTO system. The buoyancy and radiation forces are expressed as:

$$\begin{aligned} f_b(t) &= -k\,z(t), \\ f_r(t) &= -m_\infty\,\ddot{z}(t) - \int_0^t c(\tau)\,\dot{z}(t-\tau)\,d\tau. \end{aligned} \tag{6}$$

Thus, the equation of motion becomes:

$$(m + m_\infty)\,\ddot{z}(t) + \int_0^t c(\tau)\,\dot{z}(t-\tau)\,d\tau + k\,z(t) = f_e(t) + f_{PTO}(t). \tag{7}$$

Assuming this equation as linear and applying the Fourier transform to convert it into the frequency domain, with $U(\omega) = \mathcal{F}\left[\dot{z}(t)\right]$ and $F_{PTO}(\omega) = -Z_{PTO}(\omega)U(\omega)$:

$$U(\omega)\left[Z_i(\omega) + Z_{PTO}(\omega)\right] = F_e(\omega), \tag{8}$$

where the intrinsic impedance is given by

$$Z_i(\omega) = C(\omega) + i\left\{\omega\left[m + M(\omega)\right] - \frac{k}{\omega}\right\}. \tag{9}$$

To maximize power absorption, the velocity of the buoy must be in phase with the excitation force, which implies:

$$Z_{PTO}(\omega) = Z_i^*(\omega). \tag{10}$$

In this way, the required coefficients for the control cases can be determined, as further detailed in Section 5.

3 MESHING STRATEGY

The use of an Octree-type meshing approach is particularly advantageous in this study, as it allows for localized refinement in the most critical regions of the domain. High resolution can be concentrated around the buoy, where hydrodynamic forces are evaluated, and along the air–water interface, where the Volume of Fluid (VOF) method requires accurate capture of free-surface dynamics. At the same time, the mesh can be rapidly coarsened away from these regions, leading to a significant reduction in the overall number of cells. This results in a highly efficient computational setup, which is especially beneficial for large domains such as long wave flumes or open-sea simulations, where resolving the entire volume with a uniform fine mesh would be prohibitively expensive.

To achieve an Octree-type meshing, the strategy was divided into two main steps. The first step was implemented through the codeStream functionality in OpenFOAM, which allows the direct generation of mesh parameters from coded expressions embedded within the input dictionaries. By specifying a series of parameters (see Table 1), this approach enables the generation of a fully Octree-like mesh, as illustrated in Fig. 1.

In a second step, it was necessary to modify the internal boundaries between planes of different refinement levels in order to merge the entire internal mesh consistently. This was carried out using an in-house Python code that replaced the original hexahedral cells with polyhedral cells. Specifically, the algorithm subdivides the coarse cell face (from the unrefined region) into four smaller faces, ensuring a perfect match with the contiguous refined cell, as shown in Fig. 2.

Symbol	Description	Symbol	Description
Resolution / global controls			
`CPH`	Smallest vertical cell count at free surface	`AR_X`	Aspect ratio $\Delta x/\Delta z$
`AR_Y`	Aspect ratio $\Delta y/\Delta z$	`W_H`	Design wave height H
`E_W_H`	Safety band beyond H (finest CPH)		
Domain size & WEC geometry / position			
`Xtot`	Domain length in x	`Ytot`	Domain width in y
`Ztot`	Domain depth in z	`Z_alfa`	Still Water Level (SWL)
`R`	WEC radius	`XCM`	WEC CM x-coordinate
`YCM`	WEC CM y-coordinate	`ZCM`	WEC CM z-coordinate
Local blocks / refinement extents			
`X_u`	x-extent upstream buoy	`Z_d8`	z-extent (8XCPH zone)
`Z_d4`	z-extent (4XCPH zone)	`Z_d2`	z-extent (2XCPH zone)
`Y_e`	y-extent where grading starts	`X_d`	x-extent where grading starts
Grading controls			
`Gradex`	Grading factor in x	`Gradey`	Grading factor in y

All extents are measured from the buoy center of mass (CM).

Table 1: Input parameters for `codeStream` to generate the Octree-like mesh.

With these steps, the procedure is complemented by the `snappyHexMesh` utility of OpenFOAM, which is used to embed the buoy geometry into the refined rectangular region highlighted in Figs. 1 and 2. This approach ensures accurate representation of the body within the locally refined mesh, while maintaining overall computational efficiency. For instance, with a refinement level equivalent to 5 cells per wave height (CPH), a wave height of 0.024 m, and a domain size of $10 \times 1.8 \times 2.5$ m, the resulting grid contains only 264,440 cells, which demonstrates the effectiveness of the proposed meshing strategy.

By contrast, a more traditional approach based solely on `blockMesh`, without the use of Octree refinement, would require approximately 409,500 cells for the same domain configuration, highlighting the significant efficiency gains achieved with the present method.

4 WAVE REFLECTION

To minimize wave reflection at the outlet boundary of the numerical domain, a damping zone was implemented in order to absorb the incident wave energy. This was achieved by modifying the continuity equation of the incompressible Navier–Stokes formulation with an additional source term that acts as a numerical beach. The damping term is only applied to the cells located within the designated absorption region at the downstream end of the domain (See Fig. 3), thus ensuring that the main flow solution remains unaffected in the rest of the computational domain. In OpenFOAM, this strategy can be implemented in a straightforward

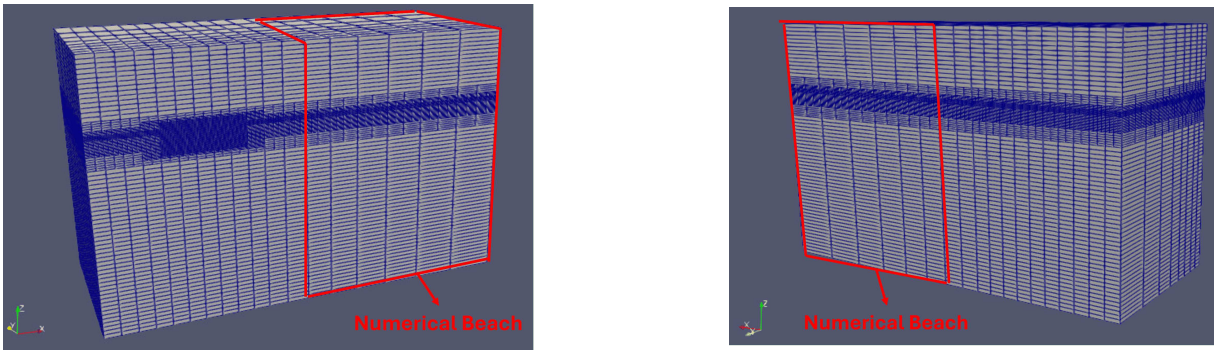

Figure 1: Front and Back view of refined Octree-like mesh.

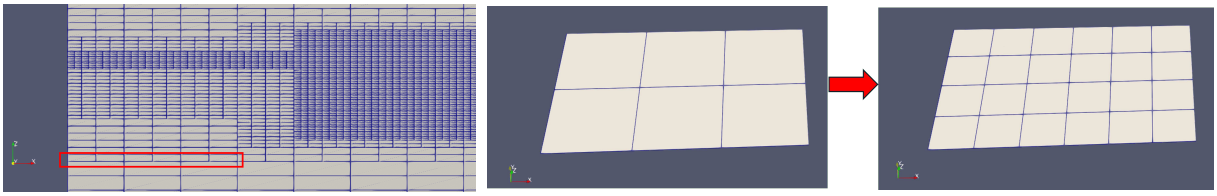

Figure 2: In-House python script boundary modification.

manner using the `fvOptions` framework. The modified continuity equation, including the additional damping term (Engsig-Karup, 2006), is given by Eq. (11) and Eq. (12).

$$\rho \frac{\partial \mathbf{v}}{\partial t} + \rho\, \mathbf{v} \cdot \nabla \mathbf{v} = -\nabla p + \nabla \cdot \left[\mu \left(\nabla \mathbf{v} + \nabla \mathbf{v}^T\right)\right] + \mathbf{b}. + \boxed{s_b \rho \mathbf{u}}. \tag{11}$$

$$s_b = -2 s_{b,\text{Max}} \left(\frac{L_B - x_b}{L_B}\right)^3 + 3 s_{b,\text{Max}} \left(\frac{L_B - x_b}{L_B}\right)^2. \tag{12}$$

Eq. (12) contains two main calibration parameters that must be adjusted depending on the type of incident wave: the length of the numerical beach L_B and the maximum damping magnitude $s_{b,\text{Max}}$. The variable x_b represents the position within the numerical beach in the direction coincident with the incident wave train. It is important to note that if $s_{b,\text{Max}}$ is chosen too large, the damping slope becomes excessively steep, which may induce spurious reflections as the wave enters the absorption zone. Conversely, increasing L_B leads to smoother damping but also increases the computational cost, since the numerical domain must be extended accordingly. For this reason, the proper calibration of these parameters is not trivial, as it requires balancing reflection minimization with computational efficiency.

To quantify wave reflection within the domain, a Python routine was developed to implement a three-point method using a least-squares fitting procedure (Mansard and Funke, 1980). The approach records free-surface elevation at three probes (See Figure 3) whose axial spacings are selected as functions of the incident wavelength, enabling separation of the measured signal into incident and reflected components. From the reconstructed spectra of both components, a reflection index I_r is obtained as the ratio between the reflected and incident spectral peak amplitudes, thus providing a robust estimate of reflection for the tested conditions.

The calibration procedure was carried out following the methodology illustrated in Fig. 4, where different values of the numerical beach length L_B were tested in combination with several magnitudes of $s_{b,\text{Max}}$. The analysis was performed under monochromatic wave conditions, using an incident wave of height 0.024 m, period 1.58 s and wavelength 3.83 m. After evaluating the different configurations, the values $s_{b,\text{Max}} = 400$ and $L_B = 2\lambda$ (two incident wavelengths) were

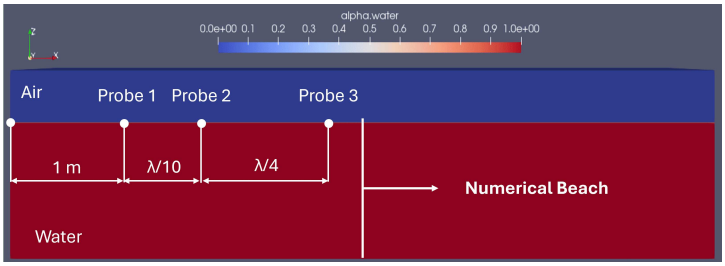

Figure 3: Wave Reflection Domain and wavee probes spacing.

selected, as they provided the best compromise between accuracy and computational efficiency. With this combination, a reflection index of only 2.3% was achieved, as can be observed in the slight variation of the free-surface elevation at probe 1 (See Figure 3), as well as in the subsequent spectral plot, both in, Fig. 5, where the difference of about fifty times between the incident ($6e^{-4}\ m^2/Hz$) and reflected ($1.3e^{-5}\ m^2/Hz$) spectral peaks is evident.

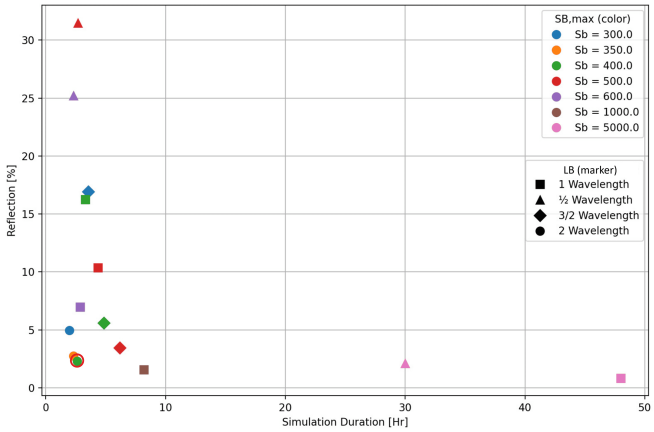

Figure 4: Reflection percentage as a function of the simulation duration for different combinations of absorbing beach lengths and $s_{b,\text{Max}}$ values. The point highlighted with a red circle indicates the selected configuration, corresponding to $s_{b,\text{Max}} = 400$ and $L_B = 2\lambda$.

5 BUOY DYNAMICS

In this section, the dynamics of the buoy are analyzed under three different scenarios: without control, with resistive control (P), and with reactive control (P+I). The resistive control (P) corresponds to a proportional strategy, where the applied force is directly proportional to the buoy velocity, effectively increasing the damping of the system. In contrast, the reactive control (P+I) adds also an integral component, which introduces a phase shift between force and velocity, allowing partial energy storage and release. This enhances the interaction with the incoming waves and can potentially increase the absorbed power.

For all cases, the numerical domain remains the same (see Fig.6), with a refinement of 5 cells per wave height (CPH) and a total of 264,440 cells. The boundary conditions and geometric dimensions were chosen to replicate the wave channel at the Faculty of Engineering of the University of Buenos Aires (FIUBA), ensuring comparability with future experimental tests. The longitudinal dimension of the tank was not fully replicated, since the numerical damping zone makes this unnecessary and avoids excessive computational cost; the 10m length shown in Fig.6 already includes the 7.66 m of the numerical beach.

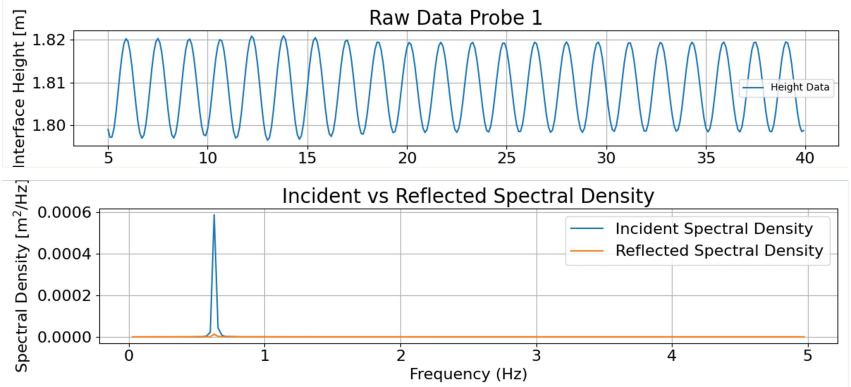

Figure 5: Raw Wave Elevation at probe 1 and Spectral Density of incident and Reflected Wave. Wave height 0.024 m, period 1.58 s and wavelength 3.83 m.

The boundary conditions are defined as follows: at the inlet, both the water volume fraction and the instantaneous velocity are prescribed using the Static Boundary Method (SBM); at the outlet, a zero-gradient condition ensures continuity and minimizes wave reflections, further reinforcing the numerical beach strategy; the front boundary is treated as a symmetry plane to reduce computational cost, while the back and bottom boundaries are modeled as no-slip walls, with the bottom representing the flume floor; the top boundary is set as atmospheric to account for the infinite air domain; and finally, the buoy surface is represented as a no-slip wall to enforce zero fluid velocity at the solid interface.

The incident waves are modeled as monochromatic waves according to first-order Airy theory, with a wave height of $H = 0.01$ m and a period of $T = 1$ s. In addition, the same numerical beach configuration chosen in Section 4 was applied here in order to test its robustness under different incident wave conditions (period and amplitude).The buoy's geometry consists of a 250 mm diameter hemisphere with a 40 mm high cylindrical section, giving it a total mass of 5.066 kg and ensuring it floats at the exact mid-height of the cylindrical section. The results of these simulations allow us to compare the influence of the different control strategies on the heave response of the buoy.

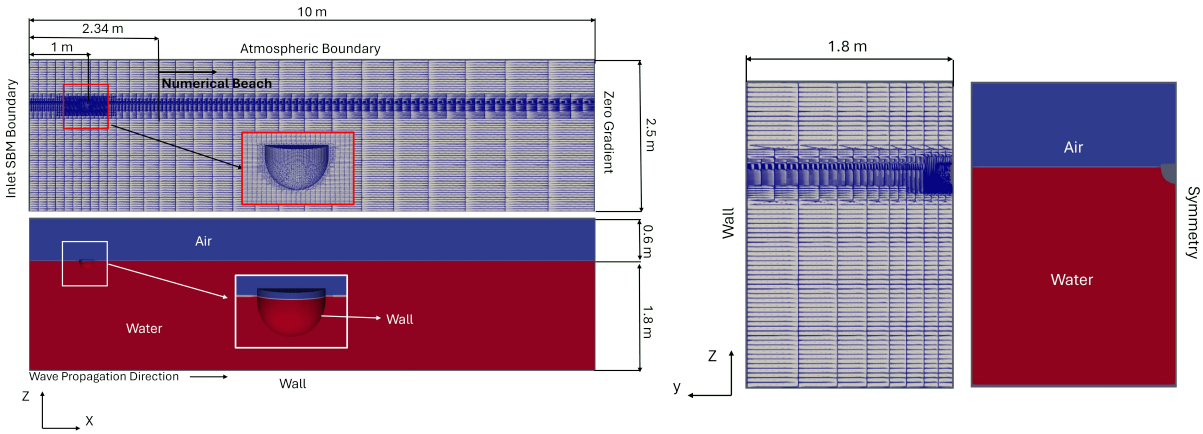

Figure 6: Buoy Dynamics Numerical Domain. Left: lateral view, right: cross plane at buoy position.

5.1 Buoy without Control

In this case, the buoy dynamics follow the formulation given in Eq. (5), with the power take-off force set to zero ($F_{PTO} = 0$).

5.2 Resistive Control Implementation

In this case, the power take-off force is modeled as a purely resistive term, expressed as

$$F_{PTO} = -B_{pto}\,\dot{z}(t), \tag{13}$$

where the value of B_{pto} is obtained from the frequency-dependent expression

$$B_{pto} = \sqrt{B_p^2 + \left(\omega_p\,[m + M_p] - \frac{k}{\omega_p}\right)^2}. \tag{14}$$

Here, M_p and B_p are the added mass and radiation damping coefficients, respectively. In this work, both quantities were extracted using the BEM open-source software `Capytaine`, and are functions of the incident wave frequency ω_p. The parameter m denotes the buoy mass. The hydrostatic stiffness coefficient k can be calculated analytically as

$$k = \rho g \pi R^2, \tag{15}$$

with R representing the buoy radius and which is valid under the assumption of a cylindrical geometry for the buoy. For the case under study, this yields a value of $k = 480.97$ N/m.

5.3 Reactive Control Implementation

In this case, the power take-off force includes both resistive and reactive components, and can be written as

$$F_{PTO} = -B_{pto}\,\dot{z}(t) - k_{pto}\,z(t). \tag{16}$$

The corresponding values of B_{pto} and k_{pto} are obtained from the following expressions:

$$B_{pto} = B_p, \tag{17}$$

$$k_{pto} = \omega_p^2\,[m + M_p] - k, \tag{18}$$

where B_p and M_p are, as before, frequency-dependent quantities obtained from `Capytaine`, and k is the hydrostatic stiffness defined previously. This formulation ensures that the reactive control accounts for both radiation and hydrostatic restoring effects, while introducing an additional stiffness term into the dynamics. In Fig. 7 wave elevation, buoy displacements, velocities, accelerations, PTO force and absorbed power, for reactive case are presented.

5.4 Results Comparison

As shown in Fig. 8, good agreement was found among the three analyzed cases (without control, with resistive control, and with reactive control) when comparing `WEC-Sim` results with those obtained from OpenFOAM. The comparison was carried out using the normalized Root Mean Squared Error (nRMSE) as the evaluation metric, which provides a consistent, dimensionless measure of the deviation between both approaches. In fact, the nRMSE values were mostly below 10% for all the evaluated variables, confirming the reliability of the methodology. It is worth noting that the discrepancy introduced by the wave height generated in OpenFOAM

tends to drive the error trends observed in the other compared quantities, highlighting the sensitivity of the results to the accuracy of the incident wave representation. Additionally, in Fig. 9, the phase space for the three buoy cases analyzed with OpenFOAM is shown. As expected, the resistive control case reduces both displacement and velocity, reflecting the extraction of energy through additional damping. In contrast, the reactive control case induces resonance in the wave–WEC system due to the inclusion of the integral (spring-like) term, which promotes phase coupling. This results in a significant increase in both displacement and velocity of the buoy.

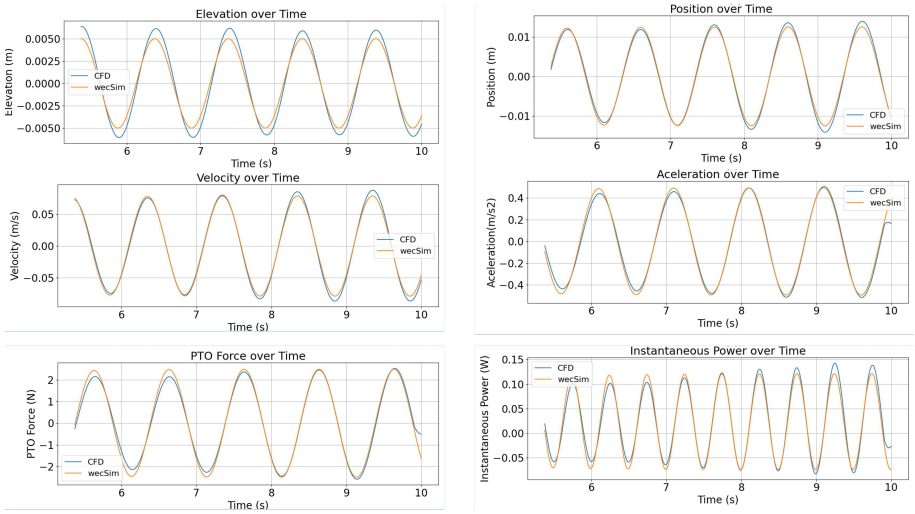

Figure 7: Reactive Control Comparison between openFOAM and `WEC-Sim` wave elevation, buoy displacements, velocities, accelerations, PTO force and absorbed power.

Without Control	
Quantity	nRMSE [%]
Wave Elevation	3.870
Buoy Displacement	8.384
Buoy Velocity	10.830
Buoy Acceleration	11.794
Total Force	12.845
Excitation Force	3.902
Radiation Damping Force	9.341
Added Mass Radiation Force	11.063
Restoring Force	7.405

Resistive Control (P)		
Quantity	nRMSE [%]	
Wave Elevation	3.650	
Buoy Displacement	3.426	
Buoy Velocity	3.425	
Buoy Acceleration	3.022	
Total Force	4.198	
Excitation Force	3.376	
Radiation Damping Force	2.798	
Added Mass Radiation Force	4.192	
Restoring Force	3.177	
PTO Force	2.529	
Instantaneous Power	6.198	
Mean Instantaneous Power [w]	CFD	0.0092
	wecSim	0.0090
Acumulated Power [J]	CFD	4.249
	wecSim	4.150

Reactive Control (PI)		
Quantity	nRMSE [%]	
Wave Elevation	7.872	
Buoy Displacement	2.997	
Buoy Velocity	2.717	
Buoy Acceleration	3.552	
Total Force	3.399	
Excitation Force	6.292	
Radiation Damping Force	3.325	
Added Mass Radiation Force	5.312	
Restoring Force	3.803	
PTO Force	3.951	
Instantaneous Power	5.952	
Mean Instantaneous Power [w]	CFD	0.0241
	wecSim	0.0212
Acumulated Power [J]	CFD	11.181
	wecSim	9.830

Figure 8: Results Comparison summary between openFOAM and `WEC-Sim` for the 3 cases analized.

6 CONCLUSIONS

The numerical strategy presented in this work allowed the efficient simulation of a point absorber buoy under controlled wave conditions. The proposed meshing methodology, complemented by an in-house boundary adjustment procedure, achieved an Octree-like refinement with a reduced cell count, ensuring computational efficiency. The introduction and calibration of a numerical beach significantly decreased unwanted wave reflections, demonstrating the importance of carefully selecting damping length and magnitude parameters. It should be noted that the present model considered only the heave degree of freedom, neglecting pitch and horizontal motions, which may become relevant in real buoy dynamics.

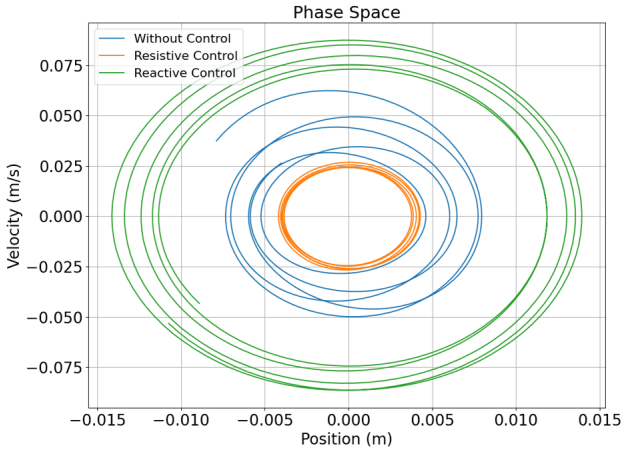

Figure 9: Phase space representation of the OpenFOAM results for the three analyzed cases.

The buoy-dynamics analysis across PTO strategies showed good agreement between OpenFOAM and potential-flow solvers (`Capytaine`, `WEC-Sim`). Resistive (P) and reactive (P+I) controls confirmed the CFD model's ability to capture both dissipative and stiffness effects, with most nRMSE values below 10%. Remaining discrepancies are largely driven by incident-wave generation errors, indicating that improved wave-calibration procedures would further enhance overall CFD accuracy. However, it should be stressed that comparisons between open-source models do not replace field measurements, and that the underlying hypotheses (e.g., laminar flow assumption, coarse mesh resolution of 5 CPH) may also contribute to differences observed between CFD and simplified solvers.

Future work will focus on extending the present methodology to nonlinear regimes, such as large-amplitude motions induced by extreme waves or sustained resonance between the wave–WEC system, as well as nonlinear effects including viscous drag, boundary-layer separation, turbulence modeling, vorticity generation, and slamming phenomena, all of which play a key role in maximizing energy capture and accurately predicting device performance.

ACKNOWLEDGEMENTS

Authors would like to thank CSC-CONICET for the computing time on TUPAC cluster, and the University of Buenos Aires for the funding received through grant 20620190100001BA.

REFERENCES

Capytaine Development Team. Capytaine: a Python-based linear potential flow BEM solver [online]. https://capytaine.org/stable/, 2025. Accessed: 2025-09-03.

Engsig-Karup A.P. *Unstructured nodal DG-FEM solution of high-order Boussinesq-type equations.* Ph.D. thesis, Technical Univeristy of Denmark, Kongens Lyngby, Ireland, 2006.

Mansard E. and Funke E. The measurement of incident and reflected spectra using a least squares method. *Coastal Engineering Proceedings*, 17:154–172, 1980. http://doi.org/10.9753/icce.v17.8.

WEC-Sim Development Team. WEC-Sim (Wave Energy Converter SIMulator) [online]. https://wec-sim.github.io/WEC-Sim/, 2025. Accessed: 2025-09-03.

Windt C. *High–fidelity numerical modelling of ocean wave energy converters*. Ph.D. thesis, Maynooth University, Maynooth, Ireland, 2020.